Fermi Arc Reconstruction in Synthetic Photonic Lattice

D.-H.-Minh Nguyen,[1,*] Chiara Devescovi,[1] Dung Xuan Nguyen,[2,†] Hai Son Nguyen,[3,4,‡] and Dario Bercioux[1,5,§]
[1]Donostia International Physics Center, 20018 Donostia-San Sebastián, Spain
[2]Center for Theoretical Physics of Complex Systems, Institute for Basic Science (IBS), Daejeon, 34126, Republic of Korea
[3]Université Lyon, Ecole Centrale de Lyon, CNRS, INSA Lyon, Université Claude Bernard Lyon 1, CPE Lyon, CNRS, INL, UMR5270, Ecully 69130, France
[4]Institut Universitaire de France (IUF), F-75231 Paris, France
[5]IKERBASQUE, Basque Foundation for Science, Euskadi Plaza, 5, 48009 Bilbao, Spain

(Received 20 November 2022; accepted 29 June 2023; published 3 August 2023)

The chiral surface states of Weyl semimetals have an open Fermi surface called a Fermi arc. At the interface between two Weyl semimetals, these Fermi arcs are predicted to hybridize and alter their connectivity. In this Letter, we numerically study a one-dimensional (1D) dielectric trilayer grating where the relative displacements between adjacent layers play the role of two synthetic momenta. The lattice emulates 3D crystals without time-reversal symmetry, including Weyl semimetal, nodal line semimetal, and Chern insulator. Besides showing the phase transition between Weyl semimetal and Chern insulator at telecom wavelength, this system allows us to observe the Fermi arc reconstruction between two Weyl semimetals, confirming the theoretical predictions.

DOI: 10.1103/PhysRevLett.131.053602

Introduction.—Weyl semimetals (WSMs) [1–3] have been at the center of intense investigation since their theoretical predictions in 2011 [4]. They are realized not only in condensed matters but also in photonic [5–15] and phononic [16–23] systems with potential applications, such as generation of optical vortex beams [13] and robust transport in the bulk medium [20]. One of the well-known signatures of WSM is the appearance of the Fermi arc (FA) surface states [4,24,25], which are chiral modes propagating unidirectionally on WSM surfaces and have an arclike Fermi surface. Topologically protected against disorder and defects [26], these FAs give rise to intriguing phenomena such as Weyl orbits [27] and magnetic domain walls with electric charge [28].

Recently, some theoretical works [29–36] predicted that at the interface between two WSMs, the surface FAs would couple to each other and be reconstructed into new interface states with different spectral shapes and bulk connections. The problem is rich since these works consider distinct junctions of WSMs. For instance, while Dwivedi *et al.* [29] examine two WSMs with the same Weyl point position and chirality, but different FA connectivity, Refs. [31,33,34] study two identical WSMs rotated from each other in their interface plane. The reconstructed FAs are expected to exhibit observable transport signatures, such as unique quantum oscillations [35] and 3D "snake states" [34]. Efforts have been made recently to fabricate a high quality interface between two chiral WSMs [37]. However, for interface states between two 3D crystals, it is challenging to directly observe their spectra using angle-resolved photoemission spectroscopy or scanning tunneling microscopy. On the other hand, the crystal surfaces are usually rough due to defects and disorders, making it difficult to fabricate a clean heterostructure, especially for the interface between rotated WSMs.

In this Letter, we propose a simple and versatile photonic lattice as the first platform to directly realize the FA reconstruction. Our system is a 1D trilayer grating where the relative displacements between layers play the role of synthetic momenta. This 1D system can simulate the topological band structure of 3D crystals with broken time-reversal (TR) symmetry, including WSM, nodal line semimetal [38,39], and 3D Chern insulator (CI) [40,41]. With our trilayer lattice, we can obtain the phase transition WSM CI just by varying the interlayer distances, or construct a photonic junction to observe the interface states between two WSMs or CIs. We will show that the interface FAs between two WSMs are strongly coupled and deformed, confirming the existence of FA reconstruction.

System and effective Hamiltonian.—We consider a slab waveguide composed of three 1D dielectric gratings that share the same subwavelength period Λ (Fig. 1). Each layer

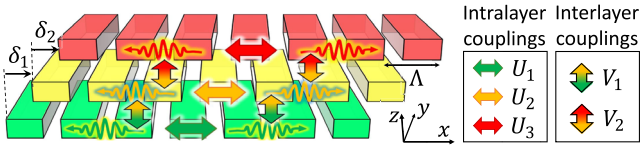

FIG. 1. Sketch of a 1D trilayer photonic grating with period Λ. The relative displacements between adjacent layers are denoted by δ_1 and δ_2. The optical guided modes of interest couple with each other via intralayer diffraction and interlayer evanescent field, described by the coupling rates U_l and V_j, respectively.

is shifted with respect to its neighbor along the grating direction by δ_j, with $j = 1, 2$. Other geometrical parameters of the lattice, including the filling fractions, grating thickness, and interlayer distances, are also of subwavelength scale. More details on the geometrical parameters for an experimental realization are presented in the Supplemental Material [42].

In each grating layer, we consider two counterpropagating guided modes along the x axis, and these modes couple to each other via the grating diffraction described by coefficients U_l, $l = 1, 2, 3$. Between adjacent layers, guided modes traveling in the same direction are coupled through the evanescent field with coupling rates V_j. Thus, our trilayer lattice has six guided modes described by the effective Hamiltonian [51–53]

$$H(k, \delta_1, \delta_2) = \begin{pmatrix} \Delta_1 & \Omega_1 & 0 \\ \Omega_1^\dagger & \Delta_2 & \Omega_2 \\ 0 & \Omega_2^\dagger & \Delta_3 \end{pmatrix}, \tag{1}$$

where $\Delta_l = \omega_{0l} + \begin{pmatrix} v_l k & U_l \\ U_l & -v_l k \end{pmatrix}$ represents the guided modes in layer l with their intralayer coupling, and $\Omega_j = \begin{pmatrix} V_j e^{-i\pi\delta_j/\Lambda} & 0 \\ 0 & V_j e^{i\pi\delta_j/\Lambda} \end{pmatrix}$ indicates the interlayer coupling. Here, v_l, ω_{0l}, and k are the group velocities, frequency offsets, and wave vector measured from the X point of the 1D BZ, respectively. The parameters ω_{0l}, v_l, and U_l are determined via the filling fraction, whereas the coupling rates V_j are retrieved from the interlayer distances of the practical structure [42].

The 1D lattice is invariant under the translations $\delta_j \to \delta_j + \Lambda$; thus, its physical properties vary periodically against δ_j. Consequently, we define the synthetic momenta proportional to the interlayer displacements [53,54] as

$$q_j = 2\pi \frac{\delta_j}{\Lambda^2}. \tag{2}$$

Such definitions hold in the presence of any perturbations that preserve the periodicity of our system. The Hamiltonian is then identified in a synthetic 3D momentum space (k, q_1, q_2), i.e., $H(k, \delta_1, \delta_2) \to H(k, q_1, q_2)$. The BZ is chosen so that $q_1, q_2 \in [0, 2\pi/\Lambda)$ [Fig. 2(a)]. Hereafter, we express the momenta in units of $2\pi/\Lambda$, frequencies in units of $2\pi c/\Lambda$, and all the coupling rates in units of $\bar{U} = 0.0207(2\pi c/\Lambda)$. Here, $\bar{U}$ is the intralayer coupling rate of a single grating with filling fraction 0.8 [42]. When all coupling rates are equal, the spectrum of this Hamiltonian shows different topological semimetallic phases—see Fig. 2(a) and solid lines of Fig. 2(b). First, bands (1) and (2), as well as bands (5) and (6), cross each other at a 3D semi-Weyl point [55–58], which disperses linearly in a 2D plane and quadratically along the direction

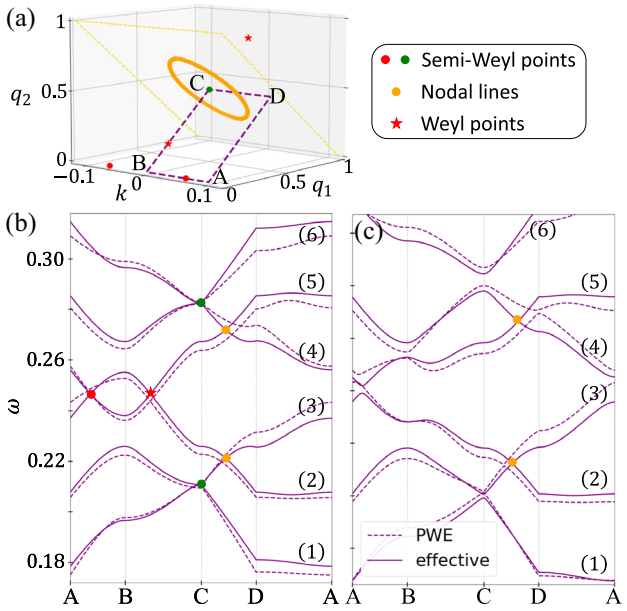

FIG. 2. (a) Nodal points and lines of the spectrum obtained from the effective model with $U_1 = U_2 = U_3 = V_1 = V_2 = 1$. They are degeneracy points of energy bands shown in (b). The violet dashed line indicates the path for plotting the band structures in (b) and (c). The band structures obtained from the effective model (solid line) and PWE simulation (dashed line) are shown for (b) $U_1 = U_2 = U_3 = V_1 = V_2 = 1$ (a), and (c) $U_1 = U_3 = 1$, $U_2 = 1.2$, $V_1 = 1.6$, and $V_2 = 0.6$. The six bands are labeled by numbers.

normal to this plane. Second, bands (2) and (3), as well as bands (4) and (5), form a nodal line [38,39] with π-Berry phase in the plane $q_1 + q_2 = 1$. Finally, bands (3) and (4) touch at two semi-Weyl points aligned along the line $q_1 = q_2 = 0$ and two Weyl points [1,2] residing in the plane $k = 0$. We can alter these nodal points and lines to obtain other phases by varying the coupling rates. For instance, the semi-Weyl points are gapped out for $U_2 > U_1 = U_3$, and the Weyl points of bands (3) and (4) are annihilated for an appropriate choice of evanescent coupling rates V_1 and V_2, as shown by the solid-line band structure of Fig. 2(c). More details about topological phases and phase transitions can be found in the Supplemental Material [42].

We validate the effective Hamiltonian by comparing its spectrum with the exact solution of Maxwell's equations, which is obtained by the plane wave expansion (PWE) method using the MIT PHOTONIC BANDS package [59]—see Figs. 2(b) and 2(c). In both cases, the two band structures agree well in the overall shape, the positions of nodal points and lines, and their gap opening. The deviations between the two approaches, which are small compared with the bandwidths, result from the coupling mechanisms neglected in our model for simplicity [42,51,60]. Hence, the effective model is an efficient tool to examine the trilayer grating.

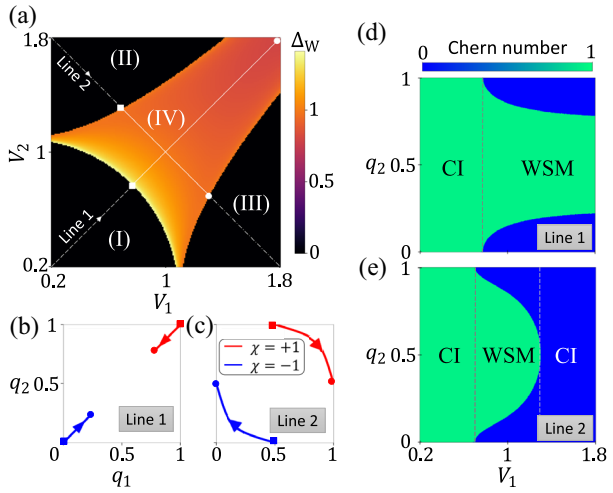

FIG. 3. (a) Distance Δ_W between the two Weyl points at $k = 0$ when $U_1 = U_3 = 1$ and $U_2 = 1.2$. The three domains in black are where bands (3) and (4) separate, and the lattice simulates a 3D CI. (b) and (c) show the Weyl point trajectories in the BZ while (d) and (e) show the Chern number computed in a 2D plane normal to q_2 when the interlayer coupling strengths vary along lines 1 and 2 of (a), respectively. In (b) and (c), χ is the Weyl point chirality.

Controlling Weyl points.—The trilayer lattice hosts topological phases owing to the synthetic momenta definition [Eq. (2)]. These momenta are proportional to the interlayer displacements and thus are even under TR, making the Hamiltonian transform as $H(k, q_1, q_2) \xrightarrow{\text{TR}} H(-k, q_1, q_2)$. Consequently, the 1D trilayer grating is equivalent to a 3D crystal with broken TR symmetry. This allows the WSM phase, which requires either inversion or TR symmetry to be broken [1]. Hereafter, we focus on the two Weyl points at $k = 0$ forming between bands (3) and (4), and thus, for simplicity, we gap out the semi-Weyl points of these bands by keeping $U_1 = U_3 = 1$ and $U_2 = 1.2$. We investigate how the Weyl points move when tuning V_1 and V_2.

The dependence of the distance between two Weyl points on the evanescent coupling rates is shown in Fig. 3(a). We define Δ_W as the distance between the Weyl points within the BZ shown in Fig. 2(a). Here, the colored domain (IV) is where the WSM phase exists, whereas the three black domains (I), (II), and (III) are where our system spectrum is gapped. The transition between WSM and insulating phases implies the annihilation of Weyl points through merging. The abrupt change in color between the domains indicates that the Weyl points meet at the BZ boundaries. To illustrate how the Weyl points move and merge, we vary the interlayer coupling rates along "line 1" and "line 2" of Fig. 3(a), and show the corresponding trajectories in Figs. 3(b) and 3(c). Following line 1, bands (3) and (4) are gapped in domain (I) until we enter the WSM domain, where two Weyl points appear at the BZ corner (0,0) and move toward each other along the diagonal ($q_1 = q_2$) as V_1 and V_2 increase. Regarding line 2, the two Weyl points appear at (0.5,0) when we go from domain (II) to (IV). They rotate about the BZ center and meet each other at (0,0.5) when the system transitions from WSM to insulator. The two Weyl points are annihilated, and bands (3) and (4) separate again. In Figs. 3(b) and 3(c), we distinguish the Weyl points by their chirality χ, which is proportional to the Berry flux threading through a surface enclosing the Weyl point. These trajectories predicted by the effective Hamiltonian [Eq. (1)] are in excellent agreement with PWE simulation [42].

Topological phases.—The Chern number is the topological invariant characterizing the bulk bands of WSMs. It can be defined for a local energy gap in 2D cross sections of the 3D BZ. Here, we consider 2D planes perpendicular to the q_2 axis and compute the Chern number in each plane as a function of q_2 [42]. The variation of Chern number following lines 1 and 2 of Fig. 3(a) are shown in Figs. 3(d) and 3(e), respectively. Along line 1, domain (I) has a nonzero Chern number over the whole BZ, suggesting a 3D CI phase. When the Weyl points appear and move toward each other, the range of q_2 with nonzero Chern number decreases and is limited between these two points. Following line 2, we also realize a CI phase in domain (II) and the WSM phase where the region between two Weyl points has a nonzero Chern number. Remarkably, domain (III) has a vanishing Chern number but is still a CI since the Chern number is now nonzero in all 2D planes normal to q_1. Such a WSM-CI transition were theoretically predicted [25,61] and observed recently in a photonic lattice for microwave frequencies [62].

Fermi arc reconstruction.—Having a lattice with a controllable WSM phase allows us to emulate the interface states between two WSMs. We consider a photonic junction of two configurations of the trilayer grating—see Fig. 4(a). The two WSMs are chosen so that the bulk spectrum of each junction side has two Weyl points, and the straight line connecting them is misaligned with the diagonal plane ($q_1 = q_2$). The Weyl points of one side can be transformed into those of the other side via reflection at the diagonal plane [Fig. 4(b)]. Hence, this photonic structure simulates the interface between two WSMs with tilted anisotropy axes. The junction's spectrum in the diagonal plane, obtained by the effective model, is shown in Fig. 4(c) (left) together with its transmission spectrum (right) simulated by the finite-difference time-domain (FDTD) method [63] using the MIT ELECTROMAGNETIC EQUATION PROPAGATION package [64]. Comparing with the effective model, which clearly distinguishes the bulk and edge states, we can discern the gapless edge states in the transmission spectrum of our junction.

To see the reconstructed FAs in an isofrequency surface, we choose a frequency close to the bulk Weyl nodes, indicated by the dashed lines in Fig. 4(c). The transmission at this frequency over the 2D synthetic BZ is shown in

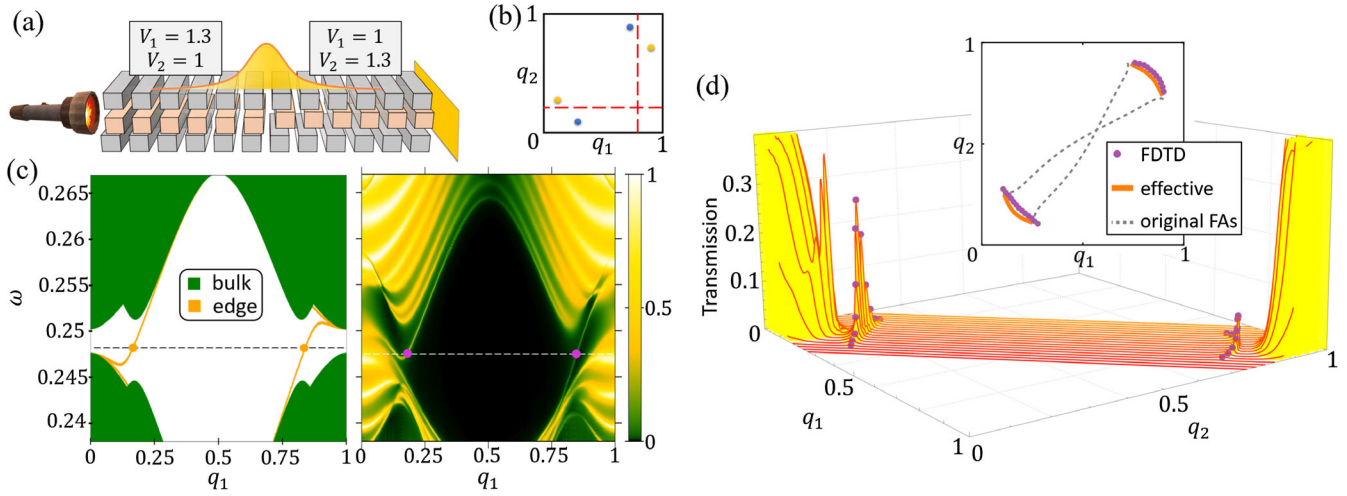

FIG. 4. Junction of two WSMs. (a) Sketch of the setup for simulation. The intralayer coupling strengths are $U_1 = U_3 = 1$ and $U_2 = 1.2$. (b) Positions of Weyl points on each side. The yellow dots correspond to $(V_1, V_2) = (1.3, 1)$ while the blue ones are for $(V_1, V_2) = (1, 1.3)$. (c) Energy spectrum of the effective model (left) and the transmission spectrum obtained from FDTD simulation (right) of the systems in the diagonal plane $q_1 = q_2$. The dashed lines indicate the frequencies for visualizing the isofrequency transmission over the synthetic BZ in (d). The inset of (d) shows the reconstructed FAs, with the dashed gray lines being the FAs before reconstruction.

Fig. 4(d), where the edge states correspond to the peaks marked by purple dots. The edge-mode transmission is strongest at $q_1 = q_2$ and dissipates toward the Weyl points, indicating the nature of FAs to connect with the bulk Weyl nodes. The resultant isofrequency contours are shown in the inset of Fig. 4(d), in agreement with the effective model. In addition, we employ the effective model to compute the original FAs of each configuration and demonstrate how they are reconstructed. We see that the two original FAs hybridize with each other and become anticrossing. Whereas the original FAs connect two Weyl points of opposite chirality on the same side, namely the same bulk, the reconstructed ones connect those with the same chirality but on different sides of the junction. This completely agrees with previous theoretical predictions [30,33,34]. The curvature of the reconstructed FAs indicates that the WSMs are strongly coupled [30,33]. Other different cases of photonic junction can be found in the Supplemental Material [42].

The reconstructed FAs are robust against perturbations since the bulk Chern number topologically protects them. Specifically, we can find cross sections of the BZ and respectively compute the Chern number on each side so that the difference in Chern number of both sides is nonzero. For instance, the cross sections parallel to k along the red dashed lines of Fig. 4(b) have a nonzero difference in Chern number. The interface FAs are thus chiral, as can be seen by the slopes of the edge states in Fig. 4(c). To describe their chiral direction, we note that the chiral direction of an original FA is given by $\mathbf{k}_W \times \mathbf{n}$, where $\mathbf{k}_W$ is the vector connecting the two Weyl points and $\mathbf{n}$ is a normal vector of the surface that goes toward the trivial media [42]. The vector $\mathbf{k}_W$ points from the source toward the sink of Berry curvature. The interface FAs are combinations of the original ones, and hence their chiral direction is given by $\Delta\mathbf{k}_W \times \mathbf{n}$, where $\Delta\mathbf{k}_W$ is the difference in $\mathbf{k}_W$ of the two sides.

Experimental feasibility.—The gratings in our system can be experimentally realized using standard nanofabrication methods, such as electron beam lithography and ionic dry etching [51,60,65]. They are made of silicon (refractive index $n = 3.46$) with period $\Lambda = 380$ nm for operation in the telecom wavelength range ($\lambda \approx 1.5$ μm). The relative displacement between the three layers can be dynamically tuned via piezoelectric actuators that are combined with goniometer stages for full control of parallelism [66–69]. Another possibility is to employ flip-chip bonding [70] to fabricate rigid structures exhibiting different relative displacements; thus measuring the structures one by one corresponds to probing the eigenmode in the (q_1, q_2) space. The edge states are visualized in far-field spectroscopy by either microreflectivity measurements [71,72], or the photoluminescence of emitters that are embedded in the gratings [73–77]. In particular, the second scenario can be used to couple edge states to single-photon emitters for quantum effects [73–75], or to an ensemble of emitters for lasing action [76,77].

Outlook.—This Letter demonstrates the FA reconstruction between two WSMs in a versatile synthetic photonic lattice. We expect that the confirmation of FA reconstruction presented here would motivate further works about phenomena related to these interface states. Moreover, this photonic system is a stepping stone to investigate not only physics in higher dimensions, such as 4D quantum

Hall effect [78] and 5D Weyl semimetal [79] but also non-Hermitian topology, which is a natural question in leaky photonic crystals when operating in the vicinity of the Γ point of the 1D BZ [60].

We kindly thank Alessandro De Martino for reading the manuscript carefully and giving us valuable comments. We are grateful for the fruitful discussions with Koji Kobayashi, Hai Chau Nguyen, and Aitzol Garcia-Etxarri. The work of D. H. M. N. and D. B. is supported by Ministerio de Ciencia e Innovación (MICINN) through Project No. PID2020–120614 GB-I00 (ENACT). D. B. thanks the support of the Transnational Common Laboratory *Quantum–ChemPhys*, the funding from the IKUR Strategy under the collaboration agreement between the Ikerbasque Foundation and DIPC on behalf of the Department of Education of the Basque Government and from the Gipuzkoa Provincial Council within the QUAN-000021-01 project. H. S. N is funded by the French National Research Agency (ANR) under the project POPEYE (No. ANR-17-CE24-0020) and the IDEXLYON from Université de Lyon, Scientific Breakthrough project TORE within the Programme Investissements d'Avenir (No. ANR-19-IDEX-0005). D. X. N. is supported by Grant No. IBS-R024-D1. C. D. acknowledges financial support from the MICIU through the FPI Ph.D. Fellowship CEX2018-000867-S-19-1.

*d.h.minh.ng@gmail.com
†dungmuop@gmail.com
‡hai-son.nguyen@ec-lyon.fr
§dario.bercioux@dipc.org

[1] N. P. Armitage, E. J. Mele, and A. Vishwanath, Weyl and Dirac semimetals in three-dimensional solids, Rev. Mod. Phys. **90**, 015001 (2018).
[2] A. Burkov, Weyl metals, Annu. Rev. Condens. Matter Phys. **9**, 359 (2018).
[3] B. Q. Lv, T. Qian, and H. Ding, Experimental perspective on three-dimensional topological semimetals, Rev. Mod. Phys. **93**, 025002 (2021).
[4] X. Wan, A. M. Turner, A. Vishwanath, and S. Y. Savrasov, Topological semimetal and Fermi-arc surface states in the electronic structure of pyrochlore iridates, Phys. Rev. B **83**, 205101 (2011).
[5] T. Dubček, C. J. Kennedy, L. Lu, W. Ketterle, M. Soljačić, and H. Buljan, Weyl Points in Three-Dimensional Optical Lattices: Synthetic Magnetic Monopoles in Momentum Space, Phys. Rev. Lett. **114**, 225301 (2015).
[6] L. Lu, Z. Wang, D. Ye, L. Ran, L. Fu, J. D. Joannopoulos, and M. Soljačić, Experimental observation of Weyl points, Science **349**, 622 (2015).
[7] Q. Lin, M. Xiao, L. Yuan, and S. Fan, Photonic Weyl point in a two-dimensional resonator lattice with a synthetic frequency dimension, Nat. Commun. **7**, 13731 (2016).
[8] J. Noh, S. Huang, D. Leykam, Y. D. Chong, K. P. Chen, and M. C. Rechtsman, Experimental observation of optical Weyl points and Fermi arc-like surface states, Nat. Phys. **13**, 611 (2017).
[9] Q. Wang, M. Xiao, H. Liu, S. Zhu, and C. T. Chan, Optical Interface States Protected by Synthetic Weyl Points, Phys. Rev. X **7**, 031032 (2017).
[10] C. Qin, Q. Liu, B. Wang, and P. Lu, Photonic Weyl phase transition in dynamically modulated brick-wall waveguide arrays, Opt. Express **26**, 20929 (2018).
[11] M. Li, J. Song, and Y. Jiang, Photonic topological Weyl degeneracies and ideal type-I Weyl points in the gyromagnetic metamaterials, Phys. Rev. B **103**, 045307 (2021).
[12] E. Lustig and M. Segev, Topological photonics in synthetic dimensions, Adv. Opt. Photonics **13**, 426 (2021).
[13] H. Cheng, W. Gao, Y. Bi, W. Liu, Z. Li, Q. Guo, Y. Yang, O. You, J. Feng, H. Sun, J. Tian, S. Chen, and S. Zhang, Vortical Reflection and Spiraling Fermi Arcs with Weyl Metamaterials, Phys. Rev. Lett. **125**, 093904 (2020).
[14] N. Han, J. Liu, Y. Gao, K. Zhou, and S. Liu, Topological phase transitions and Weyl semimetal phases in chiral photonic metamaterials, New J. Phys. **24**, 053052 (2022).
[15] W. Song, S. Wu, C. Chen, Y. Chen, C. Huang, L. Yuan, S. Zhu, and T. Li, Observation of Weyl Interface States in Non-Hermitian Synthetic Photonic Systems, Phys. Rev. Lett. **130**, 043803 (2023).
[16] M. Xiao, W.-J. Chen, W.-Y. He, and C. T. Chan, Synthetic gauge flux and Weyl points in acoustic systems, Nat. Phys. **11**, 920 (2015).
[17] F. Li, X. Huang, J. Lu, J. Ma, and Z. Liu, Weyl points and Fermi arcs in a chiral phononic crystal, Nat. Phys. **14**, 30 (2017).
[18] H. Ge, X. Ni, Y. Tian, S. K. Gupta, M.-H. Lu, X. Lin, W.-D. Huang, C. T. Chan, and Y.-F. Chen, Experimental Observation of Acoustic Weyl Points and Topological Surface States, Phys. Rev. Appl. **10**, 014017 (2018).
[19] X. Fan, C. Qiu, Y. Shen, H. He, M. Xiao, M. Ke, and Z. Liu, Probing Weyl Physics with One-Dimensional Sonic Crystals, Phys. Rev. Lett. **122**, 136802 (2019).
[20] V. Peri, M. Serra-Garcia, R. Ilan, and S. D. Huber, Axial-field-induced chiral channels in an acoustic Weyl system, Nat. Phys. **15**, 357 (2019).
[21] Z. Wang, Z. Wang, H. Li, J. Luo, X. Wang, Z. Liu, and H. Yang, Weyl points and nodal lines in acoustic synthetic parameter space, Appl. Phys. Express **14**, 077002 (2021).
[22] H. Zhang, S. Zhang, J. Liu, and B. Liu, Synthetic Weyl points of the shear horizontal guided waves in one-dimensional phononic crystal plates, Appl. Sci. **12**, 167 (2021).
[23] J.-j. Liu, Z.-w. Li, Z.-G. Chen, W. Tang, A. Chen, B. Liang, G. Ma, and J.-C. Cheng, Experimental Realization of Weyl Exceptional Rings in a Synthetic Three-Dimensional Non-Hermitian Phononic Crystal, Phys. Rev. Lett. **129**, 084301 (2022).
[24] G. Xu, H. Weng, Z. Wang, X. Dai, and Z. Fang, Chern Semimetal and the Quantized Anomalous Hall Effect in $HgCr_2Se_4$, Phys. Rev. Lett. **107**, 186806 (2011).
[25] A. A. Burkov and L. Balents, Weyl Semimetal in a Topological Insulator Multilayer, Phys. Rev. Lett. **107**, 127205 (2011).
[26] E. Witten, Three lectures on topological phases of matter, Riv. Nuovo Cimento **39**, 313–370 (2016).

[27] A. C. Potter, I. Kimchi, and A. Vishwanath, Quantum oscillations from surface Fermi arcs in Weyl and Dirac semimetals, Nat. Commun. **5**, 5161 (2014).
[28] Y. Araki, A. Yoshida, and K. Nomura, Universal charge and current on magnetic domain walls in Weyl semimetals, Phys. Rev. B **94**, 115312 (2016).
[29] V. Dwivedi, Fermi arc reconstruction at junctions between Weyl semimetals, Phys. Rev. B **97**, 064201 (2018).
[30] H. Ishida and A. Liebsch, Fermi arc engineering at the interface between two Weyl semimetals, Phys. Rev. B **98**, 195426 (2018).
[31] G. Murthy, H. A. Fertig, and E. Shimshoni, Surface states and arcless angles in twisted Weyl semimetals, Phys. Rev. Res. **2**, 013367 (2020).
[32] N. B. M. Schröter, S. Stolz, K. Manna, F. de Juan, M. G. Vergniory, J. A. Krieger, D. Pei, T. Schmitt, P. Dudin, T. K. Kim, C. Cacho, B. Bradlyn, H. Borrmann, M. Schmidt, R. Widmer, V. N. Strocov, and C. Felser, Observation and control of maximal Chern numbers in a chiral topological semimetal, Science **369**, 179 (2020).
[33] F. Abdulla, S. Rao, and G. Murthy, Fermi arc reconstruction at the interface of twisted Weyl semimetals, Phys. Rev. B **103**, 235308 (2021).
[34] F. Buccheri, R. Egger, and A. De Martino, Transport, refraction, and interface arcs in junctions of Weyl semimetals, Phys. Rev. B **106**, 045413 (2022).
[35] S. Kaushik, I. Robredo, N. Mathur, L. M. Schoop, S. Jin, M. G. Vergniory, and J. Cano, Transport signatures of Fermi arcs at twin boundaries in Weyl materials, arXiv:2207.14109.
[36] F. Bonasera, S.-B. Zhang, L. Privitera, and F. M. D. Pellegrino, Tunable interface states between floquet-Weyl semimetals, Phys. Rev. B **106**, 195115 (2022).
[37] N. Mathur, F. Yuan, G. Cheng, S. Kaushik, I. Robredo, M. G. Vergniory, J. Cano, N. Yao, S. Jin, and L. M. Schoop, Atomically sharp internal interface in a chiral Weyl semimetal nanowire, Nano Lett. **23**, 2695 (2023).
[38] A. A. Burkov, M. D. Hook, and L. Balents, Topological nodal semimetals, Phys. Rev. B **84**, 235126 (2011).
[39] C. Fang, H. Weng, X. Dai, and Z. Fang, Topological nodal line semimetals, Chin. Phys. B **25**, 117106 (2016).
[40] R. Yu, W. Zhang, H.-J. Zhang, S.-C. Zhang, X. Dai, and Z. Fang, Quantized anomalous Hall effect in magnetic topological insulators, Science **329**, 61 (2010).
[41] D. Vanderbilt, *Berry Phases in Electronic Structure Theory* (Cambridge University Press, Cambridge, England, 2018).
[42] See Supplemental Material at http://link.aps.org/supplemental/10.1103/PhysRevLett.131.053602 for additional information and data, which includes Refs. [43–50].
[43] K. Okamoto, *Fundamentals of Optical Waveguides*, 3rd ed. (Academic Press, San Diego, CA, 2021).
[44] C. Devescovi, M. García-Díez, I. Robredo, M. B. de Paz, J. Lasa-Alonso, B. Bradlyn, J. L. Mañes, M. G. Vergniory, and A. García-Etxarri, Cubic 3D Chern photonic insulators with orientable large Chern vectors, Nat. Commun. **12**, 7330 (2021).
[45] C. Devescovi, M. García-Díez, B. Bradlyn, J. L. Mañes, M. G. Vergniory, and A. García-Etxarri, Vectorial bulk-boundary correspondence for 3D photonic Chern insulators, Adv. Opt. Mater. **10**, 2200475 (2022).
[46] F. D. M. Haldane, Berry Curvature on the Fermi Surface: Anomalous Hall Effect as a Topological Fermi-Liquid Property, Phys. Rev. Lett. **93**, 206602 (2004).
[47] B. I. Halperin, Possible states for a three-dimensional electron gas in a strong magnetic field, Jpn. J. Appl. Phys. **26**, 1913 (1987).
[48] J.-P. Berenger, A perfectly matched layer for the absorption of electromagnetic waves, J. Comput. Phys. **114**, 185 (1994).
[49] R. Winkler, *Spin—Orbit Coupling Effects in Two-Dimensional Electron and Hole Systems* (Springer Berlin Heidelberg, 2003).
[50] Per-Olov Löwdin, A note on the quantum-mechanical perturbation theory, J. Chem. Phys. **19**, 1396 (1951).
[51] H. S. Nguyen, F. Dubois, T. Deschamps, S. Cueff, A. Pardon, J.-L. Leclercq, C. Seassal, X. Letartre, and P. Viktorovitch, Symmetry Breaking in Photonic Crystals: On-Demand Dispersion from Flatband to Dirac Cones, Phys. Rev. Lett. **120**, 066102 (2018).
[52] D. X. Nguyen, X. Letartre, E. Drouard, P. Viktorovitch, H. C. Nguyen, and H. S. Nguyen, Magic configurations in moiré superlattice of bilayer photonic crystals: Almost-perfect flatbands and unconventional localization, Phys. Rev. Res. **4**, L032031 (2022).
[53] H. C. Nguyen, D. X. Nguyen, T. Louvet, X. Letartre, P. Viktorovitch, and H. S. Nguyen, Topological Properties of Photonic Bands with Synthetic Momentum, arXiv:2111.02843.
[54] K. Y. Lee, K. W. Yoo, S. Cheon, W.-J. Joo, J. W. Yoon, and S. H. Song, Synthetic Topological Nodal Phase in Bilayer Resonant Gratings, Phys. Rev. Lett. **128**, 053002 (2022).
[55] S. Murakami and S.-i. Kuga, Universal phase diagrams for the quantum spin Hall systems, Phys. Rev. B **78**, 165313 (2008).
[56] C. He, S.-Y. Yu, H. Wang, H. Ge, J. Ruan, H. Zhang, M.-H. Lu, and Y.-F. Chen, Hybrid Acoustic Topological Insulator in Three Dimensions, Phys. Rev. Lett. **123**, 195503 (2019).
[57] N. Mohanta, J. M. Ok, J. Zhang, H. Miao, E. Dagotto, H. N. Lee, and S. Okamoto, Semi-Dirac and Weyl fermions in transition metal oxides, Phys. Rev. B **104**, 235121 (2021).
[58] R. Li, P. Li, Y. Jia, and Y. Liu, Self-localized topological states in three dimensions, Phys. Rev. B **105**, L201111 (2022).
[59] S. G. Johnson and J. D. Joannopoulos, Block-iterative frequency-domain methods for Maxwell's equations in a planewave basis, Opt. Express **8**, 173 (2001).
[60] X. Letartre, S. Mazauric, S. Cueff, T. Benyattou, H. S. Nguyen, and P. Viktorovitch, Analytical non-Hermitian description of photonic crystals with arbitrary lateral and transverse symmetry, Phys. Rev. A **106**, 033510 (2022).
[61] Y. Yoshimura, W. Onishi, K. Kobayashi, T. Ohtsuki, and K.-I. Imura, Comparative study of Weyl semimetal and topological/Chern insulators: Thin-film point of view, Phys. Rev. B **94**, 235414 (2016).
[62] G.-G. Liu, Z. Gao, Q. Wang, X. Xi, Y.-H. Hu, M. Wang, C. Liu, X. Lin, L. Deng, S. A. Yang, P. Zhou, Y. Yang, Y. Chong, and B. Zhang, Topological Chern vectors in three-dimensional photonic crystals, Nature (London) **609**, 925 (2022).

[63] A. Taflove and S. Hagness, *Computational electrodynamics*, 3rd ed., Artech House Antennas and Propagation Library (Artech House, Norwood, MA, 2005).
[64] A. F. Oskooi, D. Roundy, M. Ibanescu, P. Bermel, J. Joannopoulos, and S. G. Johnson, Meep: A flexible free-software package for electromagnetic simulations by the FDTD method, Comput. Phys. Commun. **181**, 687 (2010).
[65] S. Cueff, F. Dubois, M. S. R. Huang, D. Li, R. Zia, X. Letartre, P. Viktorovitch, and H. S. Nguyen, Tailoring the local density of optical states and directionality of light emission by symmetry breaking, IEEE J. Sel. Topics Quantum Electron. **25**, 1 (2019).
[66] S. Dufferwiel, F. Fras, A. Trichet, P. M. Walker, F. Li, L. Giriunas, M. N. Makhonin, L. R. Wilson, J. M. Smith, E. Clarke, M. S. Skolnick, and D. N. Krizhanovskii, Strong exciton-photon coupling in open semiconductor microcavities, Appl. Phys. Lett. **104**, 192107 (2014).
[67] F. Li, Y. Li, Y. Cai, P. Li, H. Tang, and Y. Zhang, Tunable open-access microcavities for solid-state quantum photonics and polaritonics, Adv. Quantum Technol. **2**, 1900060 (2019).
[68] Z. Geng, K. J. H. Peters, A. A. P. Trichet, K. Malmir, R. Kolkowski, J. M. Smith, and S. R. K. Rodriguez, Universal Scaling in the Dynamic Hysteresis, and Non-Markovian Dynamics, of a Tunable Optical Cavity, Phys. Rev. Lett. **124**, 153603 (2020).
[69] S. Vadia, J. Scherzer, H. Thierschmann, C. Schäfermeier, C. Dal Savio, T. Taniguchi, K. Watanabe, D. Hunger, K. Karraï, and A. Högele, Open-cavity in closed-cycle cryostat as a quantum optics platform, PRX Quantum **2**, 040318 (2021).
[70] H. Tang, B. Lou, F. Du, M. Zhang, X. Ni, W. Xu, R. Jin, S. Fan, and E. Mazur, Experimental probe of twist angle-dependent band structure of on-chip optical bilayer photonic crystal, Sci Adv. **9**, eadh8498 (2023).
[71] L. Ferrier, H. S. Nguyen, C. Jamois, L. Berguiga, C. Symonds, J. Bellessa, and T. Benyattou, Tamm plasmon photonic crystals: From bandgap engineering to defect cavity, APL Photonics **4**, 106101 (2019).
[72] N. Parappurath, F. Alpeggiani, L. Kuipers, and E. Verhagen, Direct observation of topological edge states in silicon photonic crystals: Spin, dispersion, and chiral routing, Sci. Adv. **6**, eaaw4137 (2020).
[73] I. García-Elcano, J. Merino, J. Bravo-Abad, and A. González-Tudela, Probing and harnessing photonic Fermi arc surface states using light-matter interactions, Sci. Adv. **9**, eadf8257 (2023).
[74] S. Barik, A. Karasahin, C. Flower, T. Cai, H. Miyake, W. DeGottardi, M. Hafezi, and E. Waks, A topological quantum optics interface, Science **359**, 666 (2018).
[75] M. J. Mehrabad, A. P. Foster, R. Dost, E. Clarke, P. K. Patil, A. M. Fox, M. S. Skolnick, and L. R. Wilson, Chiral topological photonics with an embedded quantum emitter, Optica **7**, 1690 (2020).
[76] Y. Ota, R. Katsumi, K. Watanabe, S. Iwamoto, and Y. Arakawa, Topological photonic crystal nanocavity laser, Commun. Phys. **1**, 86 (2018).
[77] D. Smirnova, A. Tripathi, S. Kruk, M.-S. Hwang, H.-R. Kim, H.-G. Park, and Y. Kivshar, Room-temperature lasing from nanophotonic topological cavities, Light Sci. Appl. **9**, 127 (2020).
[78] B. A. Bernevig and T. L. Hughes, *Topological Insulators and Topological Superconductors* (Princeton University Press, Princeton, NJ, 2013).
[79] B. Lian and S.-C. Zhang, Five-dimensional generalization of the topological Weyl semimetal, Phys. Rev. B **94**, 041105(R) (2016).